Received: 18 September 2020 | Revised: 10 January 2021 | Accepted: 10 February 2021

DOI: 10.1002/jor.25010

RESEARCH ARTICLE

Journal of Orthopaedic Research®

Artificial intelligence and CT-based 3D statistical modeling to assess transsacral corridors and plan implant positioning

Lukas Kamer[1] | Hansrudi Noser[1] | Charlotte Arand[2] | Kristin Handrich[2] | Pol Maria Rommens[2] | Daniel Wagner[2]

[1]AO Research Institute Davos, Davos, Switzerland

[2]Department of Orthopaedics and Traumatology, University Medical Center, Mainz, Germany

Correspondence
Charlotte Arand, University Medical Center Mainz, Department of Orthopaedics and Traumatology, Langenbeckstr. 1, 55131 Mainz, Germany.
Email: charlotte.arand@unimedizin-mainz.de

Funding information
AO Foundation

Abstract

Transsacral corridors at levels S1 and S2 represent complex osseous spaces allowing percutaneous fixation of non- or minimally-displaced fragility fractures of the sacrum. To safely place transsacral implants, they must be completely intraosseous. However, standard radiographs and CT do not properly demonstrate the corridor's intricate configuration. Our goal was to facilitate the three-dimensional assessment of transsacral corridors using artificial intelligence and the planning of transsacral implant positioning. In total, 100 pelvic CTs (49 women, mean age: 58.6 ± SD 14.8 years; 51 men, mean age: 60.7 ± SD 13 years) were used to compute a 3D statistical model of the pelvic ring. On the basis of morphologic features (=predictors) and principal components scores (=response), regression learners were interactively trained, validated, and tuned to predict/sample personalized 3D pelvic models. They were matched via thin-plate spline transformation to a series of 20 pelvic CTs with fragility fractures of the sacrum (18 women and 2 men, age: 69–9.5 years, mean age: 78.65 ± SD 8.4 years). These models demonstrated the availability, dimension, cross-section, and symmetry of transsacral corridors S1 and S2, as well as the planned implant position, dimension, axes, and entry and exit points. The complete intraosseous pathway was controlled in CT reconstructions. We succeeded to establish a workflow determining transsacral corridors S1 and S2 using artificial intelligence and 3D statistical modeling.

KEYWORDS

3D statistical model, artificial intelligence, machine learning, pelvic fracture, personalized orthopedic trauma surgery

1 | INTRODUCTION

Fragility fractures of the sacrum (FFS) show an increasing incidence in elderly; they are related to osteoporosis, usually caused by low-energy trauma, and are often associated with fractures of the anterior pelvic ring.[1–3] Typically, these fractures are non- or minimally-displaced and located lateral to the sacral foramina.[4]

Non-displaced FFS are treated with weight-bearing as tolerated and analgesics.[5] To minimize immobility-associated complications, surgical treatment is indicated in patients with immobilizing pain, ongoing restriction of mobility, and displaced fractures of the posterior pelvic ring. transsacral implants can be used to overcome the shortcomings of decreased bone mass and hence weaker screw anchorage in the sacrum of the elderly; they

are placed through transsacral corridors (TSC) at level S1 or S2.[1,6–9]

Also in high-energy lesions of the posterior pelvic ring, especially in unstable injuries, transsacral implants are used.[10] Displacement of fractures lead to a limited space for transsacral implants and should be reduced before the use of transsacral implants.[11]

These intraosseous spaces at the upper part of the posterior pelvic ring are complex and demonstrate a high anatomic variability.[9,12–14] Starting at the lateral posterior ilium, they pass the neighbored ilio-sacral joint and traverse the sacrum to reach the contralateral ilio-sacral joint and ilium. They exhibit a tubular configuration with an ovoid cross-section.[9] Their dimensions extend from a nonexisting corridor to corridors large enough to position multiple transsacral implants.[15]

The radiographic assessment of TSC S1 and S2 is impeded by the complex three-dimensional (3D) structure of TSC,[14] especially when the visibility of osseous structures is reduced as in osteoporosis. Manual image segmentation to generate 3D pelvic models is time-consuming (duration: about 3–4 h), whereas automatic segmentation is complicated by the imprecise definition of cortical borders in osteoporotic bone. Hence, minimal-invasive implant positioning at TSC S1 and S2 is challenged by difficult preoperative assessment, therapeutic decision-making, implant planning, and intraoperative implant positioning.

Artificial intelligence (AI) performs tasks that match or exceed human performance using algorithms governed by pattern recognition and self-correction.[16] Machine learning algorithms model intelligent behavior (analysis, interpretation, and comprehension of complicated information including medical and healthcare data) with minimal human intervention.[17,18] A wide variety of different machine learning algorithms are applied in different medical disciplines.[19]

3D statistical modeling is a computational technique to spatially assess specified configuration and variation patterns such as in bone models. A computed tomography (CT)-based 3D statistical model of the pelvic ring (SMPR) is a model derived from a series of pelvic CTs that comprises inherent information about 3D size, shape, and variation patterns of this skeletal site. We have been computing such models for different anatomical regions and purposes.[20–23]

The goal of this study was to improve and accelerate preoperative planning and visualization of transsacral implant positioning using artificial intelligence (especially machine learning) and 3D statistical modeling. This may help in preoperative planning and could be transferred to intraoperative visualization or navigation.

2 | METHODS

2.1 | Acquisition of pelvic CTs of patients affected by FFS

A retrospective series of 20 pelvic CTs of patients affected by non- or minimally-displaced FFS, acquired at the department of orthopedics and traumatology, University Medical Center was used; 18 women and 2 men with a mean age of 78.65 years (±SD 8.4, 69–95 years). The pelvic CTs were obtained during routine clinical diagnostic procedures for purposes unrelated to this study using standard CT scanners and imaging protocols. FFP classification by Rommens and Hofmann[24] revealed three FFP type IIa, nine type IIb, three type IIc and five type IVb. Data were available in anonymized DICOM (Digital Imaging and Communications in Medicine) format. These 18 pelvic CTs exhibited an image resolution ≤1 mm in *x*, *y*, and *z* axes. In two CTs, image resolution in the *z*-axis was 2 and 2.5 mm, respectively. CT acquisition dates ranged from March 2007 to October 2012. Ethics approval was obtained from the local respective ethics committee for the pelvic CTs to be used for the present study.

2.2 | Collecting pelvic CTs from the CT database of the AO Research Institute Davos

A total of one hundred pelvic CTs of uninjured adult European women and men were taken from AO Research Institute Davos's (ARI) CT database, registered at the "Eidgenössischer Öffentlichkeits- und Datenschutzbeauftragter" (EDÖP).[25] They were obtained from a consecutive series of 124 clinical CT scans, and 24 were excluded due to bony pathology, fractures, or lumbosacral transitional vertebrae.

All patients agreed to anonymous research use of their CT data, which have been obtained for clinical reasons. The CT images consisted of 49 women pelvic CTs with a mean age of 58.6 ± SD 14.8 years (range: 20–86 years) and 51 men pelvic CTs with a mean age of 60.7 ± SD 13 years (range: 25–85 years).

2.3 | Software and hardware environment

All pelvic CT data were transferred in DICOM format to standard laptop computers and loaded to amira software (amira version 2019.4, Thermo Fisher Scientific). Amira is a commercial software package for scientific data visualization and analysis. The capabilities of amira were extended by TCL scripting and modules written in C++. Further data processing and analysis were carried out using MATLAB's statistics and machine learning toolbox (The MathWorks GmbH). In particular, we used its regression and classification learner apps to optimize the workflow. Interested readers can look at corresponding MATLAB documentation.[26] draw.io (JGraph Ltd) was used to design diagrams.

3 | WORKFLOW

3.1 | Computing of the SMPR

The 100 uninjured pelvic CTs were used to generate an SMPR (Figure 1). Computations were made according to a method described by Arand et al.[22] The pelvic models consisted of the bony

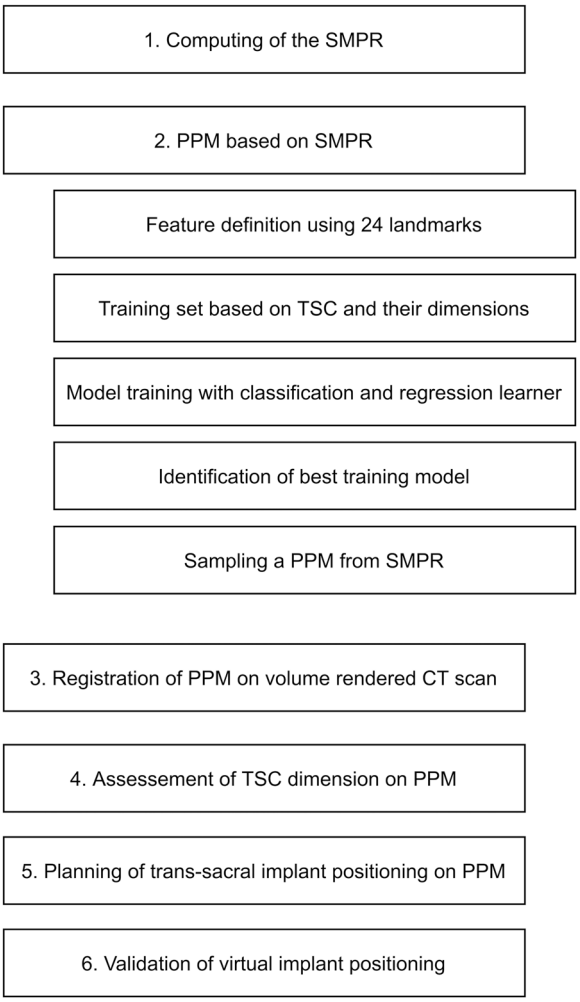

FIGURE 1 Workflow: Single steps of the presented workflow to help in transsacral corridor assessment. CT, computed tomography; PPM, personalized 3D pelvic model; SMPR, 3D statistical model of the pelvic ring; TSC, transsacral corridor

surfaces including the sacral canal and sacral neuroforamina, and cancellous bone structure was not further considered.

3.2 | Use of AI for sampling a personalized 3D pelvic model from the SMPR, comprising five main tasks

3.2.1 | Definition of features

A set of 24 landmarks was manually positioned on the mean model of the SMPR (Figure 2). On the basis of previous experience with pelvic modeling,[22,27] the landmarks were determined and distributed among the entire pelvic ring with an emphasis on the posterior pelvic ring. They were positioned at prominent anatomical sites. In particular, they were placed at the left and right pubic symphysis (2), ischial tuberosity (2), anterior, superior iliac spine (2), tubercle of iliac crest (2), ilio-sacral joint (8), posterior wing of ilium (2), and medially at the anterior and posterior sacrum (6). These landmarks were transferred to the individual pelvic models included in the SMPR according to their homologous surfaces with equal numberings and location of triangular vertices. The landmarks were used to define features, also termed predictors. They comprised distance and angle measurements between the landmarks.

3.2.2 | Definition of responses of the training set

TSC S1 and S2 of the SMPR (=training set) were evaluated with respect to their diameter. This was achieved by manual measurement of the diameters of all training set models (n = 100) in a semi-transparent lateral view using a dedicated Amira Script Object. In addition, principal components (PC) scores of the SMPR correlating well with the diameters of S1 corridors were determined, which served as responses for machine learning to find optimal learners. In MATLAB, the form coordinates or scores of all training set models in form space spanned by the PCs were correlated with the corresponding TSC S1 diameters to obtain the most important PCs for modeling the corridors. This allows to sample 3D pelvic models from the SMPR using predicted scores.

3.2.3 | Model training

Features and binary responses were transferred to MATLAB's Classification Learner APP. Confusion matrices, scatter plots, AUC values, and ROC curves were calculated and analyzed (Figure 3). The accuracy values obtained by applying 10-fold cross-validation were used to assess the learners. Features and continuous responses were transferred to MATLAB's regression learner. We interactively trained, validated, and tuned classification models for the binary existence of S1 corridors and regression models for the numeric PC scores and the S1 diameter as responses. Models were trained using supervised machine learning. Predictor variables were the features. Response variables were the binary existences of S1 corridors, the S1 corridor diameter, and the PC scores as mentioned above.

3.2.4 | Identification of the best training model

After model training, the best training model was identified on the basis of accuracies and AUC values for binary learners, and the performance score of a regression model as given by the root mean square error (RMSE) on the validation set.

3.2.5 | Sampling a PPM

On the basis of feature values, the five main PC scores were predicted with the corresponding five best learners/predictors. With these PC scores, an entire personalized 3D pelvic model (PPM) was sampled from the SMPR, using them as form coordinates in the form subspace given by the five PCs. Such a PPM from predicted scores should match the

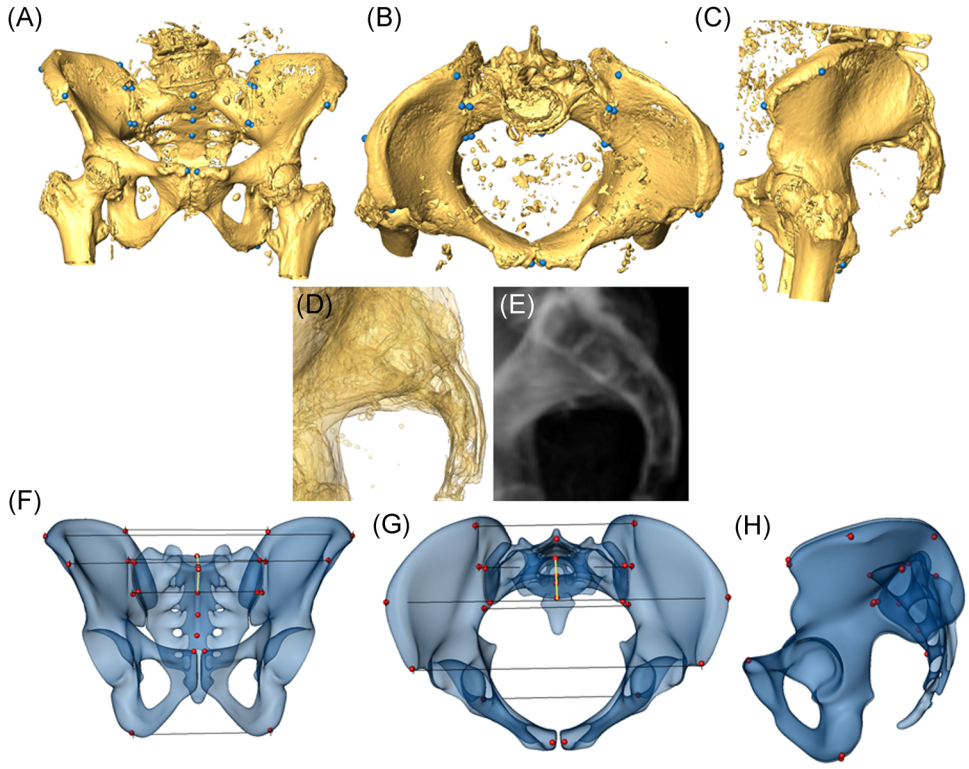

FIGURE 2 Position of landmarks and visualization of transsacral corridor (TSC) S1 and S2: Volume-rendered 3D pelvic model of an individual CT (case 011) in a.p. (A), inlet (B), and lateral view (C) with 24 homologous landmarks (blue dots). 3D pelvic model in semi-transparent lateral view (D) and digitally reconstructed radiograph (E) demonstrating the difficult visualization of TSC S1 and S2. Mean model of the 3D statistical model (SMPR) in a.p. (F), inlet (G), and lateral semitransparent view (H) with 24 homologous landmarks (red dots) and features (distances [black lines] and angles [yellow lines]). TSC S1 and S2 and their boundaries are clearly visible (H) [Color figure can be viewed at wileyonlinelibrary.com]

original pelvis (not in the training set) and can be used to determine the corridor location and existence of a corridor. They were evaluated with the PPMs in a semitransparent lateral view.

3.3 | Registration of the PPM and clinical CT case

A total number of 23 homologous landmarks were manually placed on a given PPM and its corresponding pelvic CT case using isosurface rendering and sagittal CT reconstruction (Figures 4 and 5). They were placed bilaterally at the posterior iliac fossa (2), superior borders of the ilio-sacral joint (2), lateral alae (2) and neuroforamina S1 and S2 (12), and medially at the anterior upper medial sacrum (3) and anterior border of the medullary canal at S1 and S2 (2) to delineate the boundaries of TSC S1 and S2. According to these landmarks, a thin-plate spline transformation (TPS) was applied to register the PPM and its corresponding pelvic CT.

3.4 | Assessment of 3D configuration of TSC S1 and S2

A PPM was positioned in a semitransparent lateral view (Figure 6). TSC S1 and S2 were evaluated with respect to the availability, shape of the cross-section, anteroposterior (a.p.) diameter, craniocaudal diameter, and location of its greatest width.[9] CT density profile and corridor length of TSC S1 were determined via virtual bone probing.[28] Additionally, the length of TSC S1 and S2 was manually measured. Furthermore, corridor axes, and orientation, and symmetry patterns of TSC S1 and S2 (left vs. right asymmetry) were evaluated.

3.5 | 3D planning of transsacral implant positioning S1 and S2

A given PPM was oriented in a semitransparent lateral view. If the craniocaudal diameter of TSC S1 and S2 was > 12 mm, a 12-mm-diameter landmark was placed on the projected implant pathway of TSC S1 or S2 (Figure 7). This landmark corresponded to a 7.3-mm-diameter transsacral implant located within a 4.7-mm safety zone.[15] If the craniocaudal diameter was between 7.3 and 12 mm, a 7.3-mm landmark (i.e., transsacral implant template without a safety zone) was positioned. No landmark and no implant template were placed at the craniocaudal corridor with a diameter ≤7.3 mm or when no transsacral corridor was available.

According to the size and position of the landmarks, transsacral implant templates with/without safety zones were positioned along the projected pathway. Implant exit points were determined thereof.

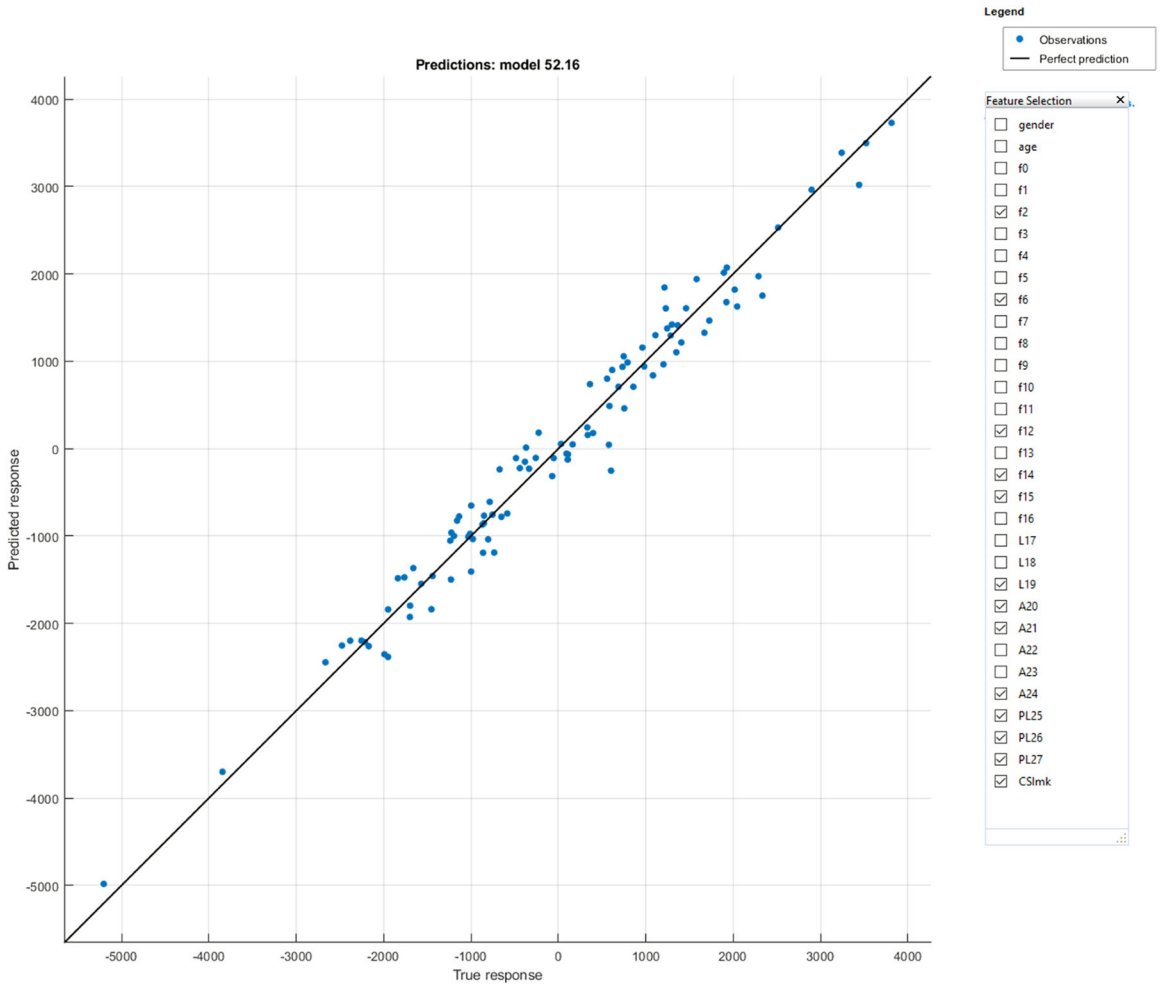

FIGURE 3 Plot of the predicted versus actual response of the PC 1 score learner. The vertical distance from the line to any point represented the error of the prediction for that point. It should be noted that in an ideal regression model, all points were to be located on a diagonal line with the predicted response equalizing the true response [Color figure can be viewed at wileyonlinelibrary.com]

3D planning of transsacral implant positioning S1 and S2 was checked via sagittal CT reconstructions. The number and position of cortical perforations were noted. 3D planning of transsacral implant positioning S1 and S2 was corrected if required. This included implant templates to be relocated and/or implant templates without safety zones to be placed.

3.6 | Validating 3D configuration of TSC S1 and S2 and 3D planning of transsacral implant positioning S1 and S2

Each PPM and its reference model (note that they were registered as described in step 3) were positioned and visualized in a semi-transparent lateral view. The cortical boundaries of TSC S1 and S2, as well as axes of the implant templates, were manually delineated.

As manual image segmentation of the reference model demonstrated to be a time-consuming task (duration: about 3–4 h per CT case), it was only performed for validation purposes. Morphometrics were compared using the *t* test.

4 | RESULTS

4.1 | Computing the SMPR

In total, 100 intact pelvic CTs were used to compute the SMPR displaying the bony surfaces of the sacrum and innominate bones including sacral neuroforamina and medullary cavity. Shape and size (=form) variations were evaluated by varying the PCs of the SMPR, as described by Arand et al.[22]: PC 1 predominantly exhibited size variation; PC 2 mainly modeled the a.p. orientation and curvature of the sacrum; and in PC 3, notable variations were observed regarding the availability or absence of TSC 1. Also, PC 3 was associated with only a moderate form of variability at TSC 2.

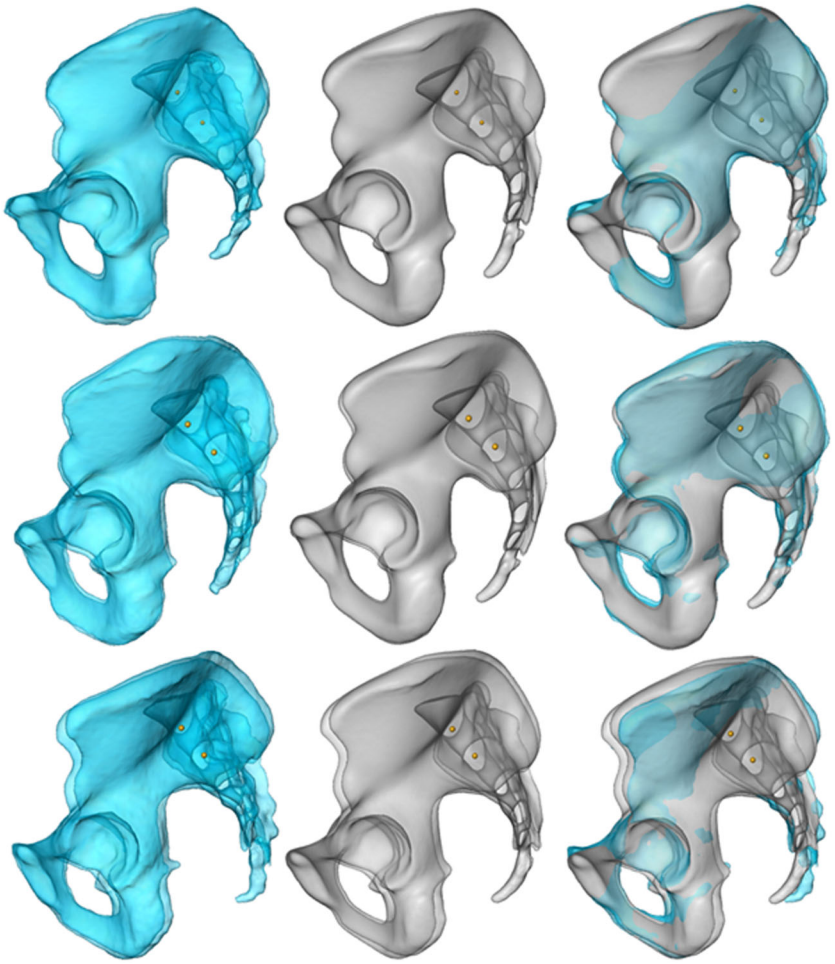

FIGURE 4 Sampling 3D pelvic models from the SMPR. Left column: Three individual 3D pelvic models (light blue models in semitransparent lateral view) of the SMPR as part of the training set; landmarks (yellow dots) indicate the position of TSC S1 and S2; middle column: sampled 3D pelvic model according to the workflow; right column: three given 3D pelvic and corresponding sampled models aligned. SMPR, 3D statistical model of the pelvic ring; TSC, transsacral corridor [Color figure can be viewed at wileyonlinelibrary.com]

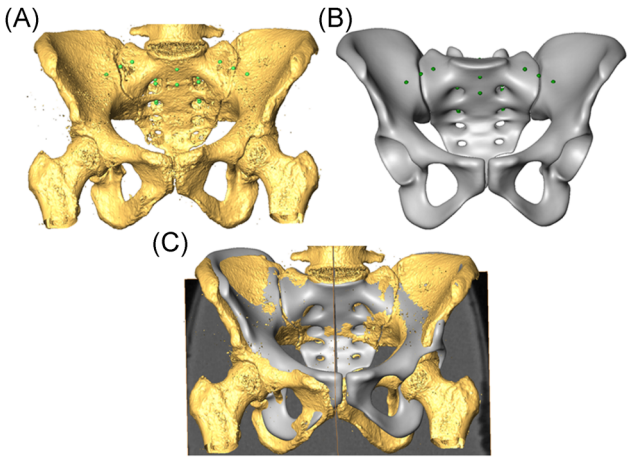

FIGURE 5 Image registration via TPS. Given 3DCT model of the pelvis (case 016, A) and corresponding PPM (B) with 23 homologous landmarks (light green and dark green dots) at TSC S1 and S2. PPM, CT, and its 3DCT model located at the same position after TPS registration (C). The optimized fit near the TSC with larger deviations in other structures as the anterior pelvic ring should be noted. CT, computed tomography; PPM, personalized 3D pelvic model; TSC, transsacral corridor [Color figure can be viewed at wileyonlinelibrary.com]

4.2 | Use of AI to sample a given PPM from the SMPR

Five different PC scores (PC 1, 2, 3, 5, and 9) were identified to be the main PCs regarding the anatomic region of TSC S1 and S2 to predict a given 3D pelvic model from the SMPR (Table 1). They were represented by five regression learners. For example, the best model for PC 1 was a Squared Exponential Gaussian Process Regression learner with a root-mean-square error (RMSE) of 265.8 and *R*-squared value of 0.97 (Figure 3). The different learner types and sets of feature variables as predictors are given in Table 1.

4.3 | Image registration

After matching the PPM to its corresponding CT, based on posteriorly localized landmarks, there was an optimized fit in the posterior pelvis at the transsacral corridors (Figure 4).

4.4 | 3D configuration of TSC S1 and S2

The corridors were assessed with the PPMs oriented in a semitransparent lateral view (Figure 6, Table 2): TSC S1 was absent in a

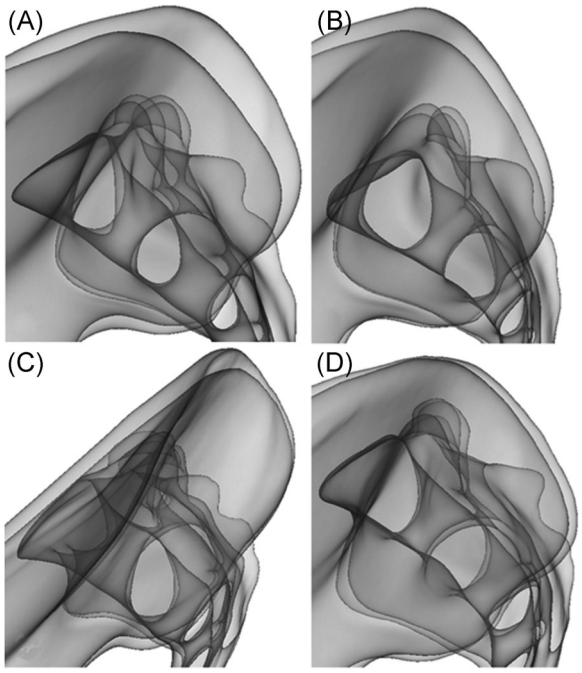

FIGURE 6 PPMs demonstrate the different 3D configuration of TSC S1 and S2: (A) asymmetric TSC S1 (case 001); (B) wide TSC S1 and S2 (case 002); (C) no TSC S1 available, wide TSC S2 (case 010); (D) ovoid TSC S1 with widest craniocaudal diameter located at the anterior center, ovoid TSC S2 with widest craniocaudal diameter situated in anterior position (case 020). TSC, transsacral corridor

single case (case 010). When available, TSC S1 and S2 displayed an overall ovoid form. However, their craniocaudal diameter and location differed notably: At TSC S1, the maximum craniocaudal diameter was situated at the anterior (2 cases), anterior-center (8 cases), and center (3 cases) location. Six cases displayed asymmetric corridor configurations exhibiting a combination of aforementioned form patterns. All PPMs exhibited a TSC S2. There, the maximum craniocaudal diameter was located at the anterior (1 case), anterior-center (7 cases), and center (9 cases). Three cases displayed notable asymmetries between the left and right sides.

4.5 | 3D planning of transsacral implant positioning S1 and S2

The procedure was performed, as exemplified in case 001 (Figure 6). In total, 38 implant templates (19 7.3-mm templates and 19 12-mm templates) were positioned. In two cases, no templates were placed at TSC S1 (cases 006 and 010). At TSC S1, seventeen 12-mm templates and two 7.3-mm templates were placed. At TSC S2, four 12-mm templates and sixteen 7.3-mm templates could be positioned. All templates were placed with the implant axes arranged in parallel orientation.

Checking 3D planning of transsacral implant positioning at S1 and S2 (Figures 8 and 9), it was observed that virtual implant positioning was associated with cortical perforations in 15 cases (75%). To avoid implant malpositioning, we relocated the implant templates in five cases (25%; three at S1 and two at S2). For the remaining cases, a smaller diameter of the implant template (7.3-mm diameter without a safe zone instead of a 12-mm diameter) was chosen. After these corrections (duration: 1–2 min per case), no cortical perforation was observed.

4.6 | Validating 3D configuration of TSC S1 and S2 and planning of transsacral implant positioning S1 and S2 thereof

In Figure 9, differences of the PPMs and manually segmented 3D pelvic models were demonstrated, which showed good correspondence.

5 | DISCUSSION

We established and validated a workflow to model TSC S1 and S2 in 3D pelvic models to analyze their spatial configuration and plan transsacral implant positioning thereof. The 3D configuration of TSC S1 and S2 was not directly evaluated in individual 2D CT images (multiplanar CT reconstructions). Instead, we integrated data of healthy individuals to generate a SMPR. It inherently contained information about 3D shape, size, and variation patterns of TSC S1 and S2. Computations were based on a previous study performed by the authors.[22] This model was used to provide a priori data in 3D for PPMs to be sampled thereof. The PPMs sampled were specified according to given pelvic CTs of patients affected by FFS. The new workflow generated was validated by comparing the PPMs with their corresponding reference models (serving as gold standard), which were processed manually using Amira's standard image segmentation tool.

Each PPM sampled was registered to its corresponding CT case according to homologous landmarks and TPS. As a result, each PPM exactly matched its corresponding CT case at sites where these landmarks were located. However, as a nonrigid registration was applied, deviations occurred in between these landmarks. These deviations were confirmed by the model validation, comparing each PPM with its corresponding reference model. Although the PPM was predicted according to features of TSC S1, it also matched TSC S2.

Only a limited number of landmarks were applied to reduce manual processing efforts: 24 homologous landmarks were placed on the entire pelvic ring for machine learning purposes and 23 additional homologous landmarks were positioned for image registration. We consider the number and position of the landmarks to be critical to obtain accurate PPMs. The use of fewer landmarks would result in a decreased manual workload; however, it would likely reduce the accuracy of the PPMs. Further research will be required to define the optimal number and position of landmarks to generate accurate PPMs.

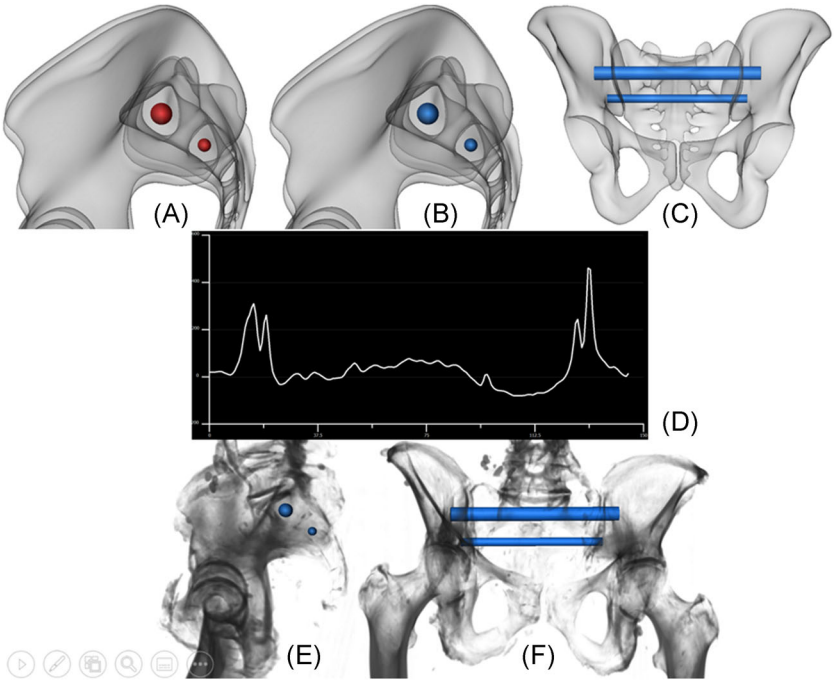

FIGURE 7 3D planning of transsacral implant positioning S1 and S2, exemplified in case 002: (A) PPM in semitransparent, lateral view with a 12-mm-diameter landmark in S1 and 7.3-mm-diameter landmark in S2 (red) at the bone entry point to define the implant pathways through TSC S1 and S2; (B) and (C) PPM in semitransparent lateral and a.p. view with a 12-mm template with a safety zone at S1 and a 7.3-mm template without a safety zone at S2; (D) virtual bone probe along transsacral corridor S1 (line curve with CT density values given in HU (*y*-axis) and bone probe length given in millimeter (*x*-axis), line probe starts at the left bone entry point; Amira's CT volume rendering in lateral (C) and a.p. view (D) with transsacral implant templates at S1 and S2 (blue); visualization is similar to fluoroscopy to transfer preoperative planning to intraoperative setup. CT, computed tomography; PPM, personalized 3D pelvic model; TSC, transsacral corridor [Color figure can be viewed at wileyonlinelibrary.com]

Irrespective of the landmarking approach and model deviations, image registration via TPS proved to be another key element of the workflow: It permitted a given PPM to be fitted and compared with its corresponding CT case and cortical perforations to be detected.

In general, TSC S1 and S2 presented a tubular configuration with an ovoid cross-section. However, we observed three main ovoid cross-section patterns depending on the location of the maximum craniocaudal diameter (center position vs. anterior position vs. position near the anterior surface of the sacrum). The different cross-section patterns may affect the implant positioning strategy and have to be considered intraoperatively.[9] Virtual bone probing may provide preoperative information about the implant holding strength.[28,29] We observed asymmetric TSC S1 and S2 with divergent corridor axes. In large TSC S1 and S2 with divergent corridor axes, implant templates may be placed with parallel or divergent implant axes, whereas in small asymmetric TSC S1 and S2, they may only be placed in divergent axis orientation.

Studying the 3D configuration of TSC S1 and S2, we confirmed the number, position, length, and diameter of the transsacral implants to be placed including their safety zones and entry and exit points. It might also be a scientific basis for transsacral implants to be placed according to well-defined, personalized criteria. They may

TABLE 1 PC 1, 2, 3, 5, and 9 regression learner characteristics

PC	Learner type	RMSE	*R*-squared	Number of predictors
1	Squared exponential Gaussian process regression (GPR)	265.8	0.97	13
2	Matern 5/2 GPR	401	0.90	15
3	Linear support vector machine (SVM)	373.8	0.83	18
5	Linear regression	309.5	0.81	19
9	Linear regression	294.9	0.56	12

TABLE 2 **Morphometrics of TSC S1 and S2 using the PPM and the reference model**. Mean ± standard deviation (range) of the corridor length, a.p., and craniocaudal diameter for TSC S1 and S2

	PPM (Personalized 3D pelvic model)	Reference model	*p* value*
a.p. diameter TSC S1	24.4 ± 6.6 (0–30)	24.2 ± 6.0 (0–29)	.921
craniocaudal diameter TSC S1	15.2 ± 5.7 (0–24)	14.8 ± 5.7 (0–21)	.826
a.p. diameter TSC S2	18.9 ± 3.0 (13–26)	17.7 ± 2.9 (13–25)	.206
craniocaudal diameter TSC S2	12.6 ± 2.7 (7–17)	13 ± 3.3 (9–24)	.677
corridor length TSC S1	148.8 ± 36.7 (0–182)	149.7 ± 36.7 (0–188)	.939
corridor length TSC S2	133.9 ± 10.5 (118–157)	138.7 ± 7.5 (124–155)	.104

Abbreviations: PPM, personalized 3D pelvic model; TSC, transsacral corridor.

*t test.

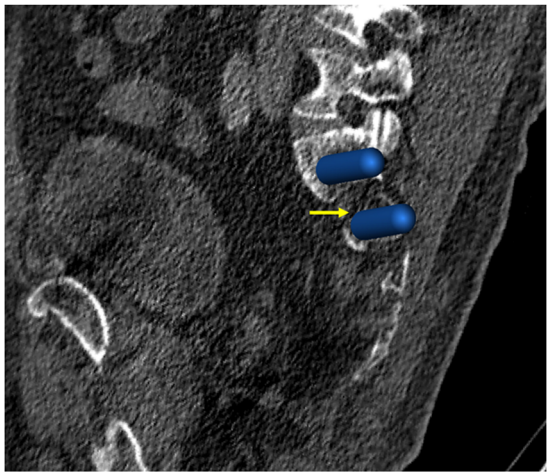

FIGURE 8 Checking 3D planning of transsacral implant positioning S1 and S2: case 004 with two 12-mm transsacral templates in TSC S1 and S2. When checking transsacral implant positioning via sagittal CT slides, a cortical perforation was observed at TSC S2, near the right neuroforamen S1 (yellow arrow). CT, computed tomography; TSC, transsacral corridor [Color figure can be viewed at wileyonlinelibrary.com]

include positioning of a single or multiple transsacral implants at S1 and/or S2 according to the cross-section pattern or bone probe profile to match the individual 3D configuration and osteoporosis status.

TSC S1 and S2 are complex anatomical structures varying in configuration (size and shape). In our study, this not only increased the risk of cortical perforation but also limited transsacral implant positioning or made it even impossible. Our finding was in accordance with previous studies where only limited space was observed, especially at S1.[9,14,15] To avoid implant malpositioning, we relocated the implant templates and used a smaller implant template diameter (implant template without a safety zone). Relocation of the implant templates and reduction of their diameter demonstrated to be successful (all templates located within the osseous boundaries of TSC S1 and S2) and effective (duration: 1–2 min per case) procedures. After checking implant positioning on preoperative multiplanar CT reconstructions, no cortical perforations were observed.

Preferably, PPMs were visualized in a semitransparent lateral view. It facilitated the assessment of TSC S1 and S2 as well as planning of the transsacral implant positioning thereof.

Our workflow was composed of multiple elements that comprised medical image data, data processing and analysis, sampling techniques based on machine learning algorithms, and image registration. We used a computer to model intelligent behavior with minimal human intervention.[17] Our study approach went beyond its contributing components to support the clinician/surgeon with new and smart information. This justifies the term AI to be used and highlights its importance for clinical evaluation, therapeutical decision-making, and treatment planning in FFS.

This study has several limitations: First, cortical perforation often occurred when only PPMs were considered. Therefore, we stress the importance of registering each PPM to its corresponding preoperative CT (multiplanar CT reconstructions) and checking virtual implant positioning thereof. Second, the time required to run the workflow was still thought to be fairly high, estimated at 15–20 min. Third, we used two CTs with low image resolution (CTs with 2 and 2.5 mm in the *z*-axis (=patient axis), compromising data processing and analysis.

Nevertheless, we think that our approach demonstrated to be beneficial over regular individual evaluations, as it allowed for the complex and highly variable TSC S1 and S2 to be mapped in 3D and for planning transsacral implant positioning thereof. More research is required to optimize the workflow described in this study (e.g., finding the optimal number and location of landmarks to be used, only including CT images with ≤1.5 mm image resolution in *x*, *y*, *z* axes (= patient axis)).

To the best of the authors' knowledge, this is the first report on AI and medical image data supporting clinical evaluation, therapeutical decision-making, and treatment planning of FFS. Similar approaches have been previously described by other authors for other purposes.[19] We acknowledge that different terms (e.g., atlas data, statistical shape models) may be used to describe features of our workflow.[30–32]

The results of this study may also be transferred to intraoperative settings to improve and facilitate intraoperative visualization and surgical handlings.[33–35] They may be applied to other injuries, medical disciplines, and/or skeletal sites. A similar approach might be chosen for ilio-sacral corridors to be assessed and for planning implant positioning thereof.[36,37]

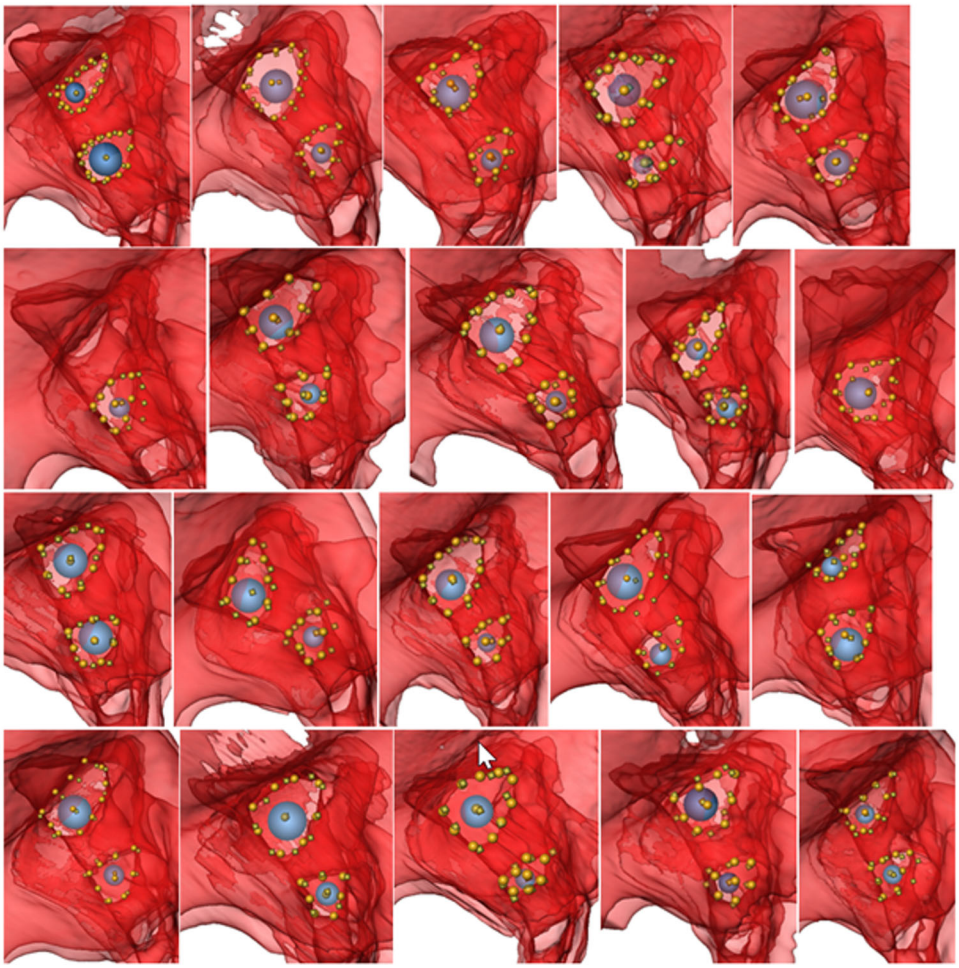

FIGURE 9 Validation of TSC S1 and S2 3D configuration and 3D planning of transsacral implant positioning S1 and S2. 1st row: cases 001–005, 2nd row: cases 006–010, 3rd row: cases 011–015, 4th row: cases 016–020 in a semitransparent lateral view. Each PPM and its reference model were located in the same anatomic orientation to demonstrate the position of the 12 and 7.3-mm templates (blue) as well as the boundary and center of TSC S1 and S2 (rectangular dots in PPMs and round dots in the reference model). TSC, transsacral corridor [Color figure can be viewed at wileyonlinelibrary.com]

6 | CONCLUSIONS

We established and validated a new workflow to model the complex and variable TSC S1 and S2 in 3D, and plan transsacral implant positioning thereof. We demonstrated the use of pelvic CTs and AI to model intelligent behavior with minimal human intervention. We assume this workflow to improve and facilitate clinical evaluation, therapeutical decision-making, and treatment planning, and lower treatment risks in patients affected by FFS. Regardless of the pros and cons of PPMs, implant positioning at TSC S1 and S2 must be directly verified via the given clinical CT to detect cortical perforations. Future studies should be targeted at defining the optimal number and position of landmarks to account for differences between the PPMs and the given clinical CT case.

ACKNOWLEDGMENTS

This study has been supported by AO Trauma, AO Foundation (project no. AR2019_01). Open Access funding enabled and organized by Projekt DEAL.

AUTHORS' CONTRIBUTION STATEMENT

Lukas Kamer initiated and conceptualized the project; acquired, processed, and analyzed the data; critically revised the manuscript. Hansrudi Noser conceptualized the project, processed and analyzed the data, and critically revised the manuscript. Charlotte Arand conceptualized the project, analyzed the data, and critically revised the manuscript. Kristin Handrich conceptualized the project, analyzed the data, and critically revised the manuscript. Pol M. Rommens conceptualized the project, acquired and analyzed the data, and critically revised the manuscript. Daniel Wagner conceptualized the project, acquired and analyzed the data, critically revised the manuscript. All the authors made a substantial contribution to this study and manuscript. All authors have read and approved the final manuscript.

ORCID

Lukas Kamer https://orcid.org/0000-0001-8173-4361
Hansrudi Noser https://orcid.org/0000-0002-8337-4416

Charlotte Arand https://orcid.org/0000-0003-3840-0299
Kristin Handrich https://orcid.org/0000-0001-7323-0585
Pol Maria Rommens https://orcid.org/0000-0002-5175-3876
Daniel Wagner https://orcid.org/0000-0003-4455-1018

REFERENCES

1. Rommens PM, Wagner D, Hofmann A. 2012. Surgical management of osteoporotic pelvic fractures: a new challenge. *Eur J Trauma Emerg Surg.* 38(5):499–509.
2. Rommens PM, Hofmann A. 2017. *Fragility Fractures of the Pelvis*. Springer, Cham. 323 p. [cited 2018 Apr 30] Available from: https://link.springer.com/chapter/10.1007/978-3-319-66572-6_3
3. Melhem E, Riouallon G, Habboubi K, Gabbas M, Jouffroy P. 2020. Epidemiology of pelvic and acetabular fractures in France. *Orthop Traumatol Surg Res.* 106(5):831–839.
4. Linstrom NJ, Heiserman JE, Kortman KE, et al. 2009. Anatomical and biomechanical analyses of the unique and consistent locations of sacral insufficiency fractures. *Spine.* 34(4):309–315.
5. Wagner D, Ossendorf C, Gruszka D, Hofmann A, Rommens PM. 2015. Fragility fractures of the sacrum: how to identify and when to treat surgically? *Eur J Trauma Emerg Surg.* 41(4):349–362.
6. Vanderschot P, Kuppers M, Sermon A, Lateur L. 2009. Trans-iliac-sacral-iliac-bar procedure to treat insufficiency fractures of the sacrum. *Indian J Orthop.* 43(3):245–252.
7. Mehling I, Hessmann MH, Rommens PM. 2012. Stabilization of fatigue fractures of the dorsal pelvis with a trans-sacral bar. Operative technique and outcome. *Injury.* 43(4):446–451.
8. Rommens PM, Ossendorf C, Pairon P, Dietz SO, Wagner D, Hofmann A. 2015. Clinical pathways for fragility fractures of the pelvic ring: personal experience and review of the literature. *J Orthop Sci.* 20(1):1–11.
9. Wagner D, Kamer L, Sawaguchi T, et al. 2017. Critical dimensions of trans-sacral corridors assessed by 3D CT models: relevance for implant positioning in fractures of the sacrum. *J Orthop Res.* 35(11):2577–2584.
10. Gardner MJ, Routt MLC Jr. 2011. Transiliac-transsacral screws for posterior pelvic stabilization. *J Orthop Trauma.* 25(6):378–384.
11. Reilly MC, Bono CM, Litkouhi B, Sirkin M, Behrens FF. 2003. The effect of sacral fracture malreduction on the safe placement of iliosacral screws. *J Orthop Trauma.* 17(2):88–94.
12. Mendel T, Noser H, Kuervers J, Goehre F, Hofmann GO, Radetzki F. 2013. The influence of sacral morphology on the existence of secure S1 and S2 transverse bone corridors for iliosacroiliac screw fixation. *Injury.* 44(12):1773–1779.
13. König MA, Sundaram RO, Saville P, Jehan S, Boszczyk BM. 2016. Anatomical considerations for percutaneous trans ilio-sacroiliac S1 and S2 screw placement. *Eur Spine J.* 25(6):1800–1805.
14. Wagner D, Kamer L, Sawaguchi T, et al. 2017. Morphometry of the sacrum and its implication on trans-sacral corridors using a computed tomography data-based three-dimensional statistical model. *Spine J.* 17(8):1141–1147.
15. Wagner D, Kamer L, Sawaguchi T, et al. 2019. Space available for trans-sacral implants to treat fractures of the pelvis assessed by virtual implant positioning. *Arch Orthop Trauma Surg.* 139(10):1385–1391.
16. Myers TG, Ramkumar PN, Ricciardi BF, Urish KL, Kipper J, Ketonis C. 2020. Artificial intelligence and orthopaedics: an introduction for clinicians. *J Bone Joint Surg Am.* 102(9):830–840.
17. Hamet P, Tremblay J. 2017. Artificial intelligence in medicine. *Metabolism.* 69S:S36–S40.
18. Peng Y, Zhang Y, Wang L. 2010. Artificial intelligence in biomedical engineering and informatics: an introduction and review. *Artif Intell Med.* 48(2–3):71–73.
19. Ranschaert ER, Morozov S, Algra PR, editors. 2019. *Artificial Intelligence in Medical Imaging: Opportunities, Applications, and Risks*. Springer International Publishing. [cited 2021 Jan 9] Available from: https://www.springer.com/gp/book/9783319948775
20. Noser H, Hammer B, Kamer L. 2010. A method for assessing 3D shape variations of fuzzy regions and its application on human bony orbits. *J Digit Imaging.* 23(4):422–429.
21. Kamer L, Noser H, Hammer B. 2013. Anatomical background for the development of preformed cranioplasty implants. *J Craniofac Surg.* 24(1):264–268.
22. Arand C, Wagner D, Richards RG, et al. 2019. 3D statistical model of the pelvic ring - a CT-based statistical evaluation of anatomical variation. *J Anat.* 234(3):376–383.
23. Maier D, Kamer L, Noser H, et al. 2012. Morphometric analysis of anatomical implant forms for minimally invasive acetabular fracture osteosynthesis. *Comput Aided Surg.* 17(5):240–248.
24. Rommens PM, Hofmann A. 2013. Comprehensive classification of fragility fractures of the pelvic ring: recommendations for surgical treatment. *Injury.* 44(12):1733–1744.
25. Messmer P, Matthews F, Jacob AL, Kikinis R, Regazzoni P, Noser H. 2007. A CT database for research, development and education: concept and potential. *J Digit Imaging.* 20(1):17–22.
26. [Date unknown]. Statistics and Machine Learning Toolbox Documentation - MathWorks Deutschland. [cited 2021 Jan 9] Available from: https://de.mathworks.com/help/stats/index.html?s_tid=CRUX_lftnav
27. Wagner D, Kamer L, Rommens PM, Sawaguchi T, Richards RG, Noser H. 2014. 3D statistical modeling techniques to investigate the anatomy of the sacrum, its bone mass distribution, and the trans-sacral corridors. *J Orthop Res.* 32(11):1543–1548.
28. Wagner D, Kamer L, Sawaguchi T, Richards RG, Noser H, Rommens PM. 2016. Sacral bone mass distribution assessed by averaged three-dimensional CT models: implications for pathogenesis and treatment of fragility fractures of the sacrum. *J Bone Joint Surg Am.* 98(7):584–590.
29. Wagner D, Hofmann A, Kamer L, et al. 2018. Fragility fractures of the sacrum occur in elderly patients with severe loss of sacral bone mass. *Arch Orthop Trauma Surg.* 138(7):971–977.
30. Baldock RA, Burger A. 2012. Biomedical atlases: systematics, informatics and analysis. *Adv Exp Med Biol.* 736:655–677.
31. Majka P, Kublik E, Furga G, Wójcik DK. 2012. Common atlas format and 3D brain atlas reconstructor: infrastructure for constructing 3D brain atlases. *Neuroinformatics.* 10(2):181–197.
32. Ambellan F, Lamecker H, von Tycowicz C, Zachow S. 2019. Statistical shape models: understanding and mastering variation in anatomy. *Adv Exp Med Biol.* 1156:67–84.
33. Bale RJ, Kovacs P, Dolati B, Hinterleithner C, Rosenberger RE. 2008. Stereotactic CT-guided percutaneous stabilization of posterior pelvic ring fractures: a preclinical cadaver study. *J Vasc Interv Radiol.* 19(7):1093–1098.
34. Thakkar SC, Thakkar RS, Sirisreetreerux N, Carrino JA, Shafiq B, Hasenboehler EA. 2017. 2D versus 3D fluoroscopy-based navigation in posterior pelvic fixation: review of the literature on current technology. *Int J Comput Assist Radiol Surg.* 12(1):69–76.
35. Rommens PM, Nolte EM, Hopf J, Wagner D, Hofmann A, Hessmann M. 2020. Safety and efficacy of 2D-fluoroscopy-based iliosacral screw osteosynthesis: results of a retrospective monocentric study. *Eur J Trauma Emerg Surg.*

36. Goetzen M, Ortner K, Lindtner RA, Schmid R, Blauth M, Krappinger D. 2016. A simple approach for the preoperative assessment of sacral morphology for percutaneous SI screw fixation. *Arch Orthop Trauma Surg*. 136(9):1251–1257.
37. Mendel T, Appelt K, Kuhn P, Suhm N. 2008. Bony sacroiliac corridor. A virtual volume model for the accurate insertion of transarticular screws. *Unfallchirurg*. 111(1):19–26.

How to cite this article: Kamer L, Noser H, Arand C, Handrich K, Rommens PM, Wagner D. Artificial intelligence and CT-based 3D statistical modeling to assess transsacral corridors and plan implant positioning. *J Orthop Res*. 2021;39: 2681–2692. https://doi.org/10.1002/jor.25010